

LETTER TO THE EDITOR

# Physical conditions in Centaurus A's northern filaments II: Does the HCO<sup>+</sup> emission highlight the presence of shocks?★

Q. Salomé<sup>1,2</sup>, P. Salomé<sup>3</sup>, B. Godard<sup>3,4</sup>, P. Guillard<sup>5</sup>, A. Gusdorf<sup>4,3</sup>

<sup>1</sup> Finnish Centre for Astronomy with ESO (FINCA), University of Turku, Vesilinnantie 5, 20014 Turku, Finland  
email: quentin.salome@utu.fi

<sup>2</sup> Aalto University Metsähovi Radio Observatory, Metsähovintie 114, 02540 Kylmäla, Finland

<sup>3</sup> Observatoire de Paris, LERMA, CNRS, Université PSL, Sorbonne Université, 75014 Paris, France

<sup>4</sup> Laboratoire de Physique de l'ENS, Ecole Normale Supérieure, Université PSL, CNRS, Sorbonne Université, 75005 Paris, France

<sup>5</sup> Sorbonne Université, CNRS, Institut d'Astrophysique de Paris, 98bis bd Arago, 75014 Paris, France

Received ??? / Accepted ??

## ABSTRACT

We present the first observation of the HCO<sup>+</sup>(1–0) and HCN(1–0) emission in the northern filaments of Centaurus A with ALMA. HCO<sup>+</sup>(1–0) is detected in 9 clumps of the Horseshoe complex, with similar velocities as the CO(1–0) emission. Conversely, the HCN(1–0) is not detected and we derive upper limits on the flux. At a resolution of ~ 40 pc, the line ratio of the velocity-integrated intensities I<sub>HCO+</sub>/I<sub>CO</sub> varies between 0.03 and 0.08, while I<sub>HCO+</sub>/I<sub>HCN</sub> is higher than unity with an average lower limit of 1.51. These ratios are significantly higher than what is observed in nearby star-forming galaxies. Moreover, the ratio I<sub>HCO+</sub>/I<sub>CO</sub> decreases with increasing CO integrated intensity, contrary to what is observed in the star-forming galaxies. This indicates that the HCO<sup>+</sup> emission is enhanced and may not arise from dense gas within the Horseshoe complex. This hypothesis is strengthened by the average line ratio I<sub>HCN</sub>/I<sub>CO</sub> < 0.03 which suggests that the gas density is rather low.

Using non-LTE, large velocity gradient modelling with RADEX, we explored two possible phases of the gas, that we call "diffuse" and "dense", and are characterised by a significant difference in the HCO<sup>+</sup> relative abundance to CO, respectively N<sub>HCO+</sub>/N<sub>CO</sub> = 10<sup>-3</sup> and N<sub>HCO+</sub>/N<sub>CO</sub> = 3 × 10<sup>-5</sup>. The average CO(1–0) and HCO<sup>+</sup>(1–0) integrated intensities and the upper limit on HCN(1–0) are compatible with both "diffuse" (n<sub>H</sub> = 10<sup>3</sup> cm<sup>-3</sup>, T<sub>kin</sub> = 15 – 165 K) and "dense" gas (n<sub>H</sub> = 10<sup>4</sup> cm<sup>-3</sup>, T<sub>kin</sub> > 65 K). The spectral setup of the present observations also covers the SiO(2–1). While undetected, the upper limit on SiO(2–1) is not compatible with the RADEX predictions for the "dense" gas. We conclude that the 9 molecular clouds detected in HCO<sup>+</sup>(1–0) are likely dominated by diffuse molecular gas. While the exact origin of the HCO<sup>+</sup>(1–0) emission remains to be investigated, it is likely related to the energy injection within the molecular gas that prevents gravitational collapse and star formation.

**Key words.** methods:data analysis - galaxies:individual:Centaurus A - galaxies:ISM - galaxies:star formation - radio lines:galaxies

## 1. Introduction

AGN are believed to play a role in regulating/quenching star formation in galaxies (Bower et al. 2006; Croton et al. 2006). However, evidence of AGN positive feedback, that enhances star formation, is also invoked in radio galaxies, in particular in regions of radio jet-gas interaction at low (Croft et al. 2006; Morganti 2010; Salomé et al. 2015; Zovaro et al. 2020; Capetti et al. 2022) and high redshift (Nesvadba et al. 2020; Duncan et al. 2023).

Centaurus A is a large double-lobes radio source that extend over about 600 kpc (see Neff et al. 2015 and references therein). About 15 kpc away from the radio core, the radio lobe emission encounters a large HI shell (Schiminovich et al. 1994), associated with recent star formation (Rejkuba et al. 2001; Auld et al. 2012; Joseph et al. 2022). Its proximity (d = 3.8 Mpc; Harris et al. 2010) makes Centaurus A the ideal target to study the impact of the AGN-driven jet on its environment. Salomé et al. (2016b,a) observed a large reservoir of molecular gas at the intersection of the radio continuum and the HI gas, within the optical northern filaments (Blanco et al. 1975; Morganti et al. 1991).

\* This paper makes use of the following ALMA data: ADS/JAO.ALMA#2015.1.01019.S, and #2016.1.00261.S.

The bulk of the molecular gas lies outside the HI shell, suggesting that the jet-gas interaction induced star formation by triggering the atomic-to-molecular gas phase transition (Salomé et al. 2016a). However, the large reservoir of molecular gas is very inefficient to form stars compare with nearby star-forming galaxies (Salomé et al. 2016b,a).

The Atacama Large submillimeter Array (ALMA) resolved the CO emission in the so-called northern filaments of Centaurus A and enabled to observe a collection of giant molecular clouds (GMC) distributed along a Horseshoe-like structure (Salomé et al. 2017). These molecular clouds have very similar physical properties (mass, size, velocity dispersion) as in the inner Milky Way. However, the virial parameter indicates that kinetic energy is injected into the molecular clouds and prevents gravitational collapse. Moreover, the excitation of the ionised gas associated with the Horseshoe complex suggests the presence of shocks (Salomé et al. 2016a, 2017) which could explain the inefficient jet-induced star formation.

Salomé et al. (2019) used mid-J CO lines observed with APEX in position 16 of Salomé et al. (2016a). Using the Paris-Durham shock model (Flower & Pineau des Forêts 2015), they showed that the CO line ratios are compatible with low-velocity shocks in diffuse gas (shock velocities between 4 – 20 km.s<sup>-1</sup>

Table 1: Summary of the ALMA and ACA observations during Cycle 3 and Cycle 4.

Species & Line	Observatory	Project	$\nu_{\text{obs}}$ (GHz)	Resolution	MRS	$\delta_{\nu}$ ( $\text{km.s}^{-1}$ )	rms (mJy/beam)
CO(1–0)	ALMA-12m	2015.1.01019.S	115.0611	$1.48'' \times 1.10''$	10.9''	1.5	4.9
CO(1–0)	ALMA+ACA	2015.1.01019.S	115.0611	$1.56'' \times 1.15''$	57.5''	1.5	4.7
HCN(1–0)	ALMA-12m	2016.1.00261.S	88.4689	$2.30'' \times 2.00''$	15.5''	3.0	0.58
HCO <sup>+</sup> (1–0)	ALMA-12m	2016.1.00261.S	89.0259	$2.29'' \times 1.99''$	15.4''	3.0	0.59
SiO(2–1)	ALMA-12m	2016.1.00261.S	86.6887	$2.35'' \times 2.03''$	15.8''	3.0	0.60

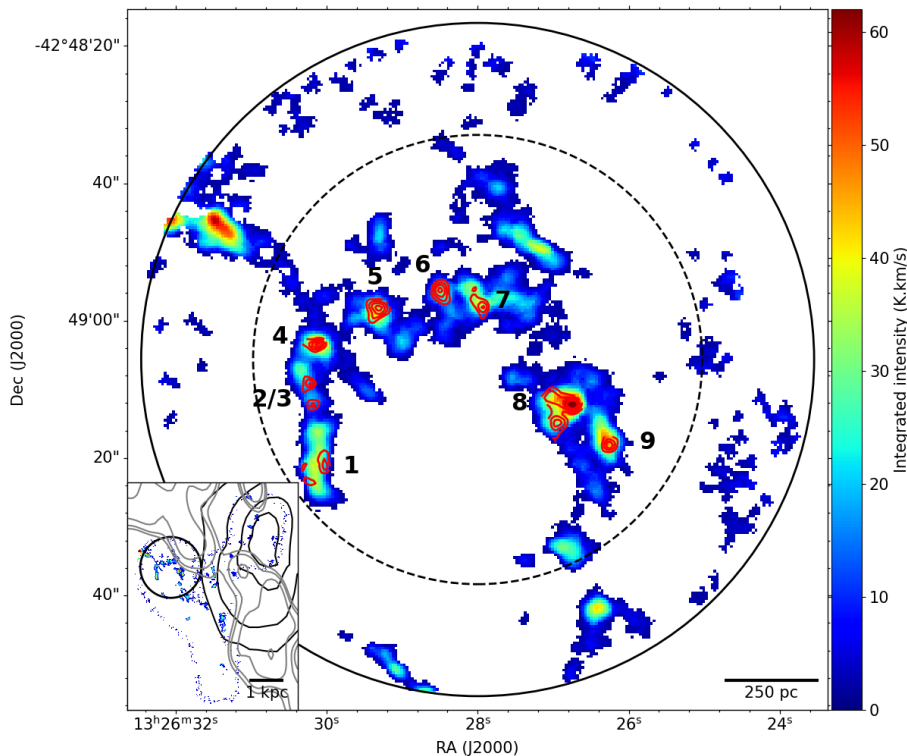


**Fig. 1.** Moment 0 map of the CO(1–0) emission at the resolution of the HCO<sup>+</sup> observations. The red contours are those of the HCO<sup>+</sup> emission. The full line and dashed circles correspond to the field of view and the FWHM of the HCO<sup>+</sup> primary beam, respectively. The numbers are the labels of the clumps. *Subpanel:* Position of the HCO<sup>+</sup> field of view with respect to the HI shell (black contours) and the radio continuum (grey contours). For a larger spatial overview, the region is indicated as "outer filament" in Fig.1 of Oosterloo & Morganti (2005).

and pre-shock density  $n_{\text{h}} = 100 \text{ cm}^{-3}$ ). However, these predictions are an average over the large area covered by the beams ( $> 250 \text{ pc}$ ). The high resolution of ALMA now allows to study the shocks experienced by the different GMC.

In this letter, we present ALMA observations of dense gas tracers (HCN, HCO<sup>+</sup>) in the Horseshoe complex and compare them with the cold molecular gas traced by CO. We aim to constrain the properties of the molecular gas when the giant molecular clouds are resolved. The data are presented in Section 2. We analyse the data in Sections 3 and 4, then compare our observations with a grid of RADEX models in Section 5.

## 2. Observations

The HCN(1–0) and HCO<sup>+</sup>(1–0) lines were observed with the ALMA 12m array during Cycle 4 using the Band 3 receivers (project 2016.1.00261.S). The observations consist in one pointing centred on the eastern CO-bright region from Salomé et al. (2016a), which was later identified as the Horseshoe complex by Salomé et al. (2017). The baselines ranged from 15.1 m to 460 m, corresponding to a resolution of  $2.1'' \times 1.6''$  and maximum recoverable scales (MRS) of about  $15.5'' \sim 280 \text{ pc}$ .

To improve the sensitivity, we decreased the spatial resolution by cutting the baseline larger than 272.6 m (corresponding to the 90th percentile), and reduced the channel sampling to  $3.0 \text{ km.s}^{-1}$ . The total integration time of 2.1 h provides a noise level of 0.58–0.59 mJy/beam in a synthesised beam of

$2.3'' \times 2.0'' \sim 42 \times 37 \text{ pc}$  (PA  $\sim 88^\circ$ ). Our observations also covered the SiO(2–1) line with a rms of 0.60 mJy/beam.

For the CO(1–0) emission, we re-calibrated, re-combined and re-imaged the observations of Salomé et al. (2017, 2019) (project 2015.1.01019.S) because an issue with CASA affected the flux in the ACA data (see the NAASC Memo 117<sup>1</sup>). We obtained a spatial resolution of  $1.56'' \times 1.15'' \sim 29 \times 21 \text{ pc}$  (PA =  $89^\circ$ ). The noise level is 4.7 mJy/beam at a spectral resolution of  $1.5 \text{ km.s}^{-1}$ .

Table 1 summarise the main characteristics of the various data cubes. The combination of ALMA and ACA for the CO(1–0) emission enables us to cover a large range of spatial scale and limit the spatial filtering by the interferometer. For HCN, HCO<sup>+</sup> and SiO, the maximum recovered scale corresponds to 280–290 pc. The HCN and HCO<sup>+</sup> emission is commonly used as a tracer of dense gas in galaxies. Moreover, in local Giant Molecular Clouds, most of the emission is localised in the densest regions (e.g. Pety et al. 2017 in Orion B). While we cannot rule out a filtering of possible extended HCN and HCO<sup>+</sup> emission, we expect the emission to be much more compact than the MRS, and the spatial filtering to be negligible. This hypothesis will be tested by comparing our results with those obtained when considering the CO(1–0) emission from ALMA alone, which has a MRS of  $10.9'' \sim 200 \text{ pc}$  closer to the MRS of HCN, HCO<sup>+</sup> and SiO.

<sup>1</sup> <https://drive.google.com/file/d/1F2LoWnJlRTdq-hRr1Pfhfz78sfdhBRzM/view>

Table 2: Properties of the different clumps detected with ALMA. The clumps numbers are the same as those indicated in Fig. 1. The integrated flux densities were derived by summing the channels where emission is detected, multiplied by the channel width. The velocity (relative to Centaurus A) and FWHM are estimated by fitting the spectrum with a single Gaussian profile. For the HCN(1–0) and SiO(2–1) emission, upper limits at  $3\sigma$  were derived assuming the same FWHM and the same area as for the HCO<sup>+</sup>(1–0). The last three columns report the line ratios of the integrated intensities in K.km.s<sup>-1</sup>, and therefore corrected by the ratio of the rest frequencies (see Section 4).

Clump	$\int S_{\text{HCO}^+} dv$ (mJy km s <sup>-1</sup> )	FWHM (km s <sup>-1</sup> )	$v_{\text{peak}}$ (km s <sup>-1</sup> )	$\int S_{\text{CO}} dv$ (Jy km s <sup>-1</sup> )	$\int S_{\text{HCN}} dv$ (mJy km s <sup>-1</sup> )	$\int S_{\text{SiO}} dv$ (mJy km s <sup>-1</sup> )	$I_{\text{HCO}^+}/I_{\text{CO}}$	$I_{\text{HCO}^+}/I_{\text{HCN}}$	$I_{\text{HCN}}/I_{\text{CO}}$
1	41.8 ± 7.2	37 ± 7	~ -206	1.23 ± 0.04	< 32.3	< 37.9	0.057 ± 0.012	> 1.28	< 0.044
2	20.0 ± 3.3	28 ± 5	~ -237	0.43 ± 0.03	< 15.7	< 15.9	0.078 ± 0.018	> 1.26	< 0.062
3	22.9 ± 4.8	24 ± 8	~ -239	0.53 ± 0.03	< 17.0	< 16.2	0.072 ± 0.019	> 1.33	< 0.054
4	42.3 ± 6.9	36 ± 5	~ -247	2.35 ± 0.07	< 38.2	< 36.3	0.030 ± 0.006	> 1.09	< 0.027
5	71.3 ± 8.7	56 ± 8	~ -257	3.38 ± 0.11	< 52.5	< 64.3	0.035 ± 0.005	> 1.34	< 0.026
6	75.6 ± 5.2	16 ± 1	~ -224	1.97 ± 0.08	< 13.3	< 15.8	0.064 ± 0.007	> 5.61	< 0.011
7	41.0 ± 4.8	23 ± 3	~ -234	1.63 ± 0.07	< 17.9	< 14.9	0.042 ± 0.007	> 2.26	< 0.019
8	194.1 ± 12.7	54 ± 3	~ -291	11.93 ± 0.26	< 89.4	< 104.0	0.027 ± 0.002	> 2.14	< 0.013
9	40.6 ± 6.6	47 ± 12	~ -267	1.91 ± 0.06	< 37.9	< 41.0	0.036 ± 0.007	> 1.06	< 0.034
Total	549.6 ± 21.5			25.36 ± 0.32	< 314.2	< 346.3	0.036 ± 0.002	> 1.73	< 0.021
Average							0.043 ± 0.018	> 1.51	< 0.029

### 3. Morpho-kinematics of the gas

#### 3.1. HCO<sup>+</sup>(1-0) emission

We first used the mapping package from the GILDAS software<sup>2</sup> to produce moment 0 maps of the HCN(1–0), HCO<sup>+</sup>(1–0) and SiO(2–1) lines. We used the velocity range of the CO(1–0) emission in this region ( $-350 < v < -175$  km s<sup>-1</sup>; Salomé et al. 2017) and a threshold of  $1.1\sigma$ . HCO<sup>+</sup> is detected while HCN and SiO are not. Using the moment 0 map of HCO<sup>+</sup>(1–0) as a guide, we explored the data cube with the viewer tool of mapping in order to constrain the velocity range of the line emission from each clump. For each clump, we then spectrally averaged the uv table over the corresponding velocity range to produce an image of the emission.

The signal-to-noise ratio of the data cube is rather low (<5 in each pixel). Therefore, we created a 3D mask in order to exclude as many channels that do not contain signal, to limit the impact of noise, and to produce more accurate moment maps of the HCO<sup>+</sup>(1–0) emission. For each clump, the mask selects the channels within the velocity range of the line emission, and the pixels within the  $2\sigma$  contours of the spectrally-integrated emission.

Figure 1 shows the moment 0 map of the CO(1–0) emission, with the contours of the HCO<sup>+</sup>(1–0) emission. The HCO<sup>+</sup> emission is distributed in 9 clumps that follow the same morphology as the CO(1–0) emission, with the Horseshoe-like feature clearly identified. Dense gas tracers have already been detected in molecular outflows (e.g. Salas et al. 2014 in M82, Alatalo 2015; Cicone et al. 2020 in Mrk 231, Walter et al. 2017 in NGC 253, Barcos-Muñoz et al. 2018 in Arp 220). However, this is the first detection of dense gas tracers in a region of jet-gas interaction.

We extracted the integrated spectrum of each clump within the  $2\sigma$  contour of this new moment 0 map. The spectra were analysed in the CLASS package of GILDAS. The spectral resolution was first decreased to 6 km s<sup>-1</sup> in order to improve the signal-to-noise ratio without undersampling the line. The integrated flux density  $\int S_{\text{HCO}^+} dv$  was derived by integrating the spectra over the velocity ranges used to build the 3D mask. For the velocity  $v_{\text{peak}}$  and FWHM, we fitted the emission by a single Gaussian. The characteristics of the HCO<sup>+</sup>(1–0) emission of each clump is reported in Table 2. The spectra are presented in Figure A.1.

<sup>2</sup> <http://www.iram.fr/IRAMFR/GILDAS>

#### 3.2. HCN(1-0) emission

The HCN(1–0) line is not detected with the present ALMA observations. Since the HCN and HCO<sup>+</sup> lines are commonly expected to trace the dense gas, we assume that the HCN(1–0) line would be emitted by the same region as the HCO<sup>+</sup>(1–0), with similar linewidths (e.g. Pety et al. 2017; Jiménez-Donaire et al. 2019). We extracted the HCN(1–0) spectrum of each clump within the  $2\sigma$  contour of the HCO<sup>+</sup>(1–0) moment 0 map and derived an upper limit at  $3\sigma$ :

$$\int S_{\text{HCN}} dv \text{ (mJy km s}^{-1}\text{)} < \frac{\sqrt{2\pi}}{2.354} \times 3\sigma \text{ (mJy)} \text{ FWHM}_{\text{HCO}^+} \quad (1)$$

where we assume  $\text{FWHM}_{\text{HCN}} = \text{FWHM}_{\text{HCO}^+}$  is the full-width at half maximum of the HCO<sup>+</sup> from Table 2. The HCN(1–0) integrated flux density is smaller than 13 – 90 mJy.km.s<sup>-1</sup>, similar to the upper limit of 33.5 mJy.km.s<sup>-1</sup> reported by Salomé et al. (2016b) from ATCA observations within the HI shell.

The SiO(2–1) line is not detected neither. Using the same method as for HCN(1–0), we derived upper limits of 16 – 104 mJy.km.s<sup>-1</sup>.

#### 3.3. CO(1-0) emission

We smoothed the CO(1–0) cube to the spatial resolution of the HCO<sup>+</sup>(1–0) and extracted the CO(1–0) spectra of the clumps within the  $2\sigma$  contour of the HCO<sup>+</sup>(1–0) moment 0 map. The CO emission covers the same range of velocities as the HCO<sup>+</sup> emission (see Figure A.1). The CO line profiles were fitted with a Gaussian profile. The integrated fluxes are reported in Table 2. The integrated fluxes obtained when considering the ALMA data alone are 10% to 30% lower (not reported in Table 2), likely due to the diffuse CO(1–0) emission.

### 4. Line ratios

In order to compare with the literature, we study the ratios of the velocity-integrated intensities  $I_{\text{CO}}$ ,  $I_{\text{HCO}^+}$  and  $I_{\text{HCN}}$ , in K.km.s<sup>-1</sup>. The line ratios of the integrated intensities of the clumps can be derived from the integrated flux densities by taking into account the rest frequency of the lines:

$$I_1/I_2 = \left( \int S_1 dv / \int S_2 dv \right) \times (v_2/v_1)^2 \quad (2)$$

where  $I_i$  are the integrated intensities,  $\int S_i dv$  are the integrated flux densities and  $\nu_i$  are the frequencies. The line ratios of each clump are reported in Table 2.

The  $I_{\text{HCO}^+}/I_{\text{CO}}$  line ratio varies between 0.03 and 0.08. This is significantly higher than what was observed in nearby star-forming galaxies by the EMPIRE (Jiménez-Donaire et al. 2019) and ALMOND surveys (Neumann et al. 2023). Moreover,  $I_{\text{HCO}^+}/I_{\text{CO}}$  decreases with increasing CO integrated intensity, contrary to what is observed in the star-forming galaxies (Figure 2 - left). This suggests that the  $\text{HCO}^+(1-0)$  emission is not tracing the dense gas within the northern filaments of Centaurus A. Instead, it looks that the  $\text{HCO}^+$  emission is enhanced by an external process that is not related to density.

For the  $I_{\text{HCN}}/I_{\text{CO}}$  and  $I_{\text{HCO}^+}/I_{\text{HCN}}$  line ratios, we derived upper and lower limits, respectively. The line ratio  $I_{\text{HCN}}/I_{\text{CO}}$  is lower than 0.06 and  $I_{\text{HCO}^+}/I_{\text{HCN}}$  is higher than unity. The average  $I_{\text{HCO}^+}/I_{\text{HCN}}$  of the clumps is  $> 1.51$ , while the  $I_{\text{HCO}^+}/I_{\text{HCN}}$  ratio of the total emission from the clumps is  $> 1.72$ . In particular, three clumps detected in  $\text{HCO}^+$  have a line ratio  $I_{\text{HCO}^+}/I_{\text{HCN}}$  higher than 2, similar to that in the nuclear region of NGC 5128 (McCoy et al. 2017). The  $I_{\text{HCO}^+}/I_{\text{HCN}}$  line ratio is significantly higher than the typical ratio observed in star-forming galaxies (Figure 2 - right; Brouillet et al. 2005; Jiménez-Donaire et al. 2019; Forbrich et al. 2023; García-Rodríguez et al. 2023; Neumann et al. 2023).

The  $I_{\text{HCO}^+}/I_{\text{HCN}}$  ratio for the total emission is typical of what is observed in starbursts (Imanishi et al. 2007; Salas et al. 2014; Schirm et al. 2016; Walter et al. 2017) or "composite" AGN associated with a nuclear starburst (Kohno 2003, 2005; Krips et al. 2008; Privon et al. 2015). Such high line ratio can also be associated with low gas metallicity (e.g. Galametz et al. 2020; Forbrich et al. 2023). However, there is no evidence of recent star formation in the Horseshoe complex and the gas metallicity is only slightly sub-solar (see Salomé et al. 2016a, 2017 and references within), suggesting that the enhanced  $\text{HCO}^+(1-0)$  emission likely has another origin.

The diffuse CO emission represents 10% to 30% of the total emission of the clumps. Therefore, if the HCN,  $\text{HCO}^+$  and SiO emission is extended and not fully recovered by ALMA, then our conclusion would be the same as the  $I_{\text{HCO}^+}/I_{\text{CO}}$  ratio would be even larger.

## 5. Low-velocity gradient modelling

We used the non-LTE radiative transfer code RADEX (van der Tak et al. 2007) to constrain the physical conditions of the clumps. Given a molecule X and the triplet  $\{N_X, n_{\text{H}}, T_{\text{kin}}\}$ , RADEX models the integrated intensities of the lines of the molecule. We adopted a linewidth  $\Delta V = 35 \text{ km.s}^{-1}$ , corresponding to the average FWHM of the clumps. The outputs of the RADEX models are compared with the average integrated intensities over the clumps:  $I_{\text{CO}} = 36.0 \pm 11.9 \text{ K.km.s}^{-1}$ ,  $I_{\text{HCO}^+} = 1.56 \pm 0.12 \text{ K.km.s}^{-1}$  and  $I_{\text{HCN}} < 1.03 \text{ K.km.s}^{-1}$ .

We explored the triplet  $\{N_X, n_{\text{H}}, T_{\text{kin}}\}$  with (i)  $n_{\text{H}} = 50, 100, 500, 10^3, 10^4 \text{ cm}^{-3}$ , (ii)  $N_{\text{CO}}$  between  $10^{15} - 10^{19} \text{ cm}^{-2}$ , and (iii) kinetic temperatures from 10 K to 200 K. We consider two phases of the gas that we will call "diffuse gas" ( $n \lesssim 500 \text{ cm}^{-3}$ ; e.g. Snow & McCall 2006) and "dense gas" ( $n \geq 10^4 \text{ cm}^{-3}$ ; e.g. Snow & McCall 2006). This two phase are characterised by typical and significantly different relative abundances  $N_{\text{HCO}^+}/N_{\text{CO}}$  and  $N_{\text{HCN}}/N_{\text{CO}}$ . We therefore derived the column density of  $\text{HCO}^+$  and HCN from their relative abundances. In the following, we adopt the relative abundances  $N_{\text{HCO}^+}/N_{\text{CO}} = 10^{-3}$  and  $N_{\text{HCN}}/N_{\text{HCO}^+} = 1.9$  (Liszt et al. 2010; Godard et al. 2010)

for the "diffuse" molecular gas,  $N_{\text{HCO}^+}/N_{\text{CO}} = 3 \times 10^{-5}$  and  $N_{\text{HCN}}/N_{\text{HCO}^+} = 1.5$  (Liszt et al. 2010; Liu et al. 2013) for the "dense" molecular gas. When running RADEX, we consider the excitation by collisions with  $\text{H}_2$ , He and the electrons. We adopt the following abundance ratios:  $n_{\text{He}}/n_{\text{H}} = 0.1$ ,  $n_{\text{e}}/n_{\text{H}} = 0, 10^{-5}, 10^{-4}$ .

The present grid of models only reproduces simultaneously the observed average integrated intensities for densities of  $10^3$  and  $10^4 \text{ cm}^{-3}$  (presented in Figure 3). The models which reproduce the observations are highlighted in red and reported in Table 3. Two regimes of the molecular gas can reproduce the observations: "dense" gas at  $n_{\text{H}} = 10^4 \text{ cm}^{-3}$  and  $T_{\text{kin}} > 65 \text{ K}$ ; "diffuse" gas at  $n_{\text{H}} = 10^3 \text{ cm}^{-3}$  and  $T_{\text{kin}} = 15 - 165 \text{ K}$ . We get the same predictions whichever the CO emission from ALMA+ACA or from ALMA alone is used. We note that the predictions for the "diffuse" gas are in agreement with the mid-J CO line ratios at lower spatial resolution from Salomé et al. (2019), which are indicated by the dotted contours in Figure 3.

Table 3: **Predictions from RADEX.** Triplets  $\{N_{\text{CO}}, n_{\text{H}}, T_{\text{kin}}\}$  that reproduce the CO and  $\text{HCO}^+$  intensities and the upper limit on HCN for the "diffuse" and "dense" gas.

$N_{\text{HCO}^+}/N_{\text{CO}}$	$n_{\text{H}}$ ( $\text{cm}^{-3}$ )	$n_{\text{e}}$ ( $\text{cm}^{-3}$ )	$N_{\text{CO}}$ ( $10^{16} \text{ cm}^{-2}$ )	$T_{\text{kin}}$ (K)
$3 \times 10^{-5}$ ("Dense" gas)	$10^4$	0	8.5–9.6	$> 104$
	$10^4$	0.1	7.9–9.6	$> 103$
	$10^4$	1	6.6–7.6	$> 65$
$10^{-3}$ ("Diffuse" gas)	$10^3$	0	2.0–4.3	19–166
	$10^3$	0.01	2.0–4.8	15–125

We explored the effects of small variations of relative abundance values around their typical estimates taken here to characterise the dense and the diffuse gas. This is illustrated in Appendix B. For the dense gas, varying the abundance does not change the possible values of the gas density, which must remain high ( $\geq 10^4 \text{ cm}^{-3}$ ). However, if the abundance is significantly reduced (by 40% or more) then there are no longer any compatible solutions at  $n = 10^4 \text{ cm}^{-3}$ . On the other hand, if the abundance is increased significantly (by 40% or more), then the possible temperature solutions tend to decrease and to become bounded. For the diffuse gas, varying the abundance does not change the possible values of the gas density either: it remains at lower densities ( $\leq 10^3 \text{ cm}^{-3}$ ). If the abundance is significantly reduced (by 40% or more) then there are again no longer any compatible solutions, even at high density. On the other hand, if the abundance is significantly increased (by 30% or more), then solutions at lower temperatures and lower densities become possible. In conclusion, abundances significantly smaller than the typical values used for the dense and diffuse here are excluded or would lead to models not compatible with our observations. On the opposite, significantly higher abundances would imply possible lower temperatures for dense gas and lower temperatures and/or lower densities for diffuse gas. It should be noted however that these conclusions are based solely on variations around characteristic abundance values for the two cases of dense and diffuse gas. A detailed study of the variation in abundance in a less constrained parameter space is not carried out here.

*SiO emission* - While  $\text{SiO}(2-1)$  is not detected, we derived upper limits (see Section 3.2 and Table 2). We investigate the effect of considering this upper limit  $I_{\text{SiO}} < 1.08 \text{ K.km.s}^{-1}$  when constraining the RADEX. To do so, we use a SiO abundance  $N_{\text{SiO}}/N_{\text{H}_2} = 10^{-8.5}$  (from Towner et al. 2024). The upper limit on SiO is indicated by the magenta line in Figure 3. This upper

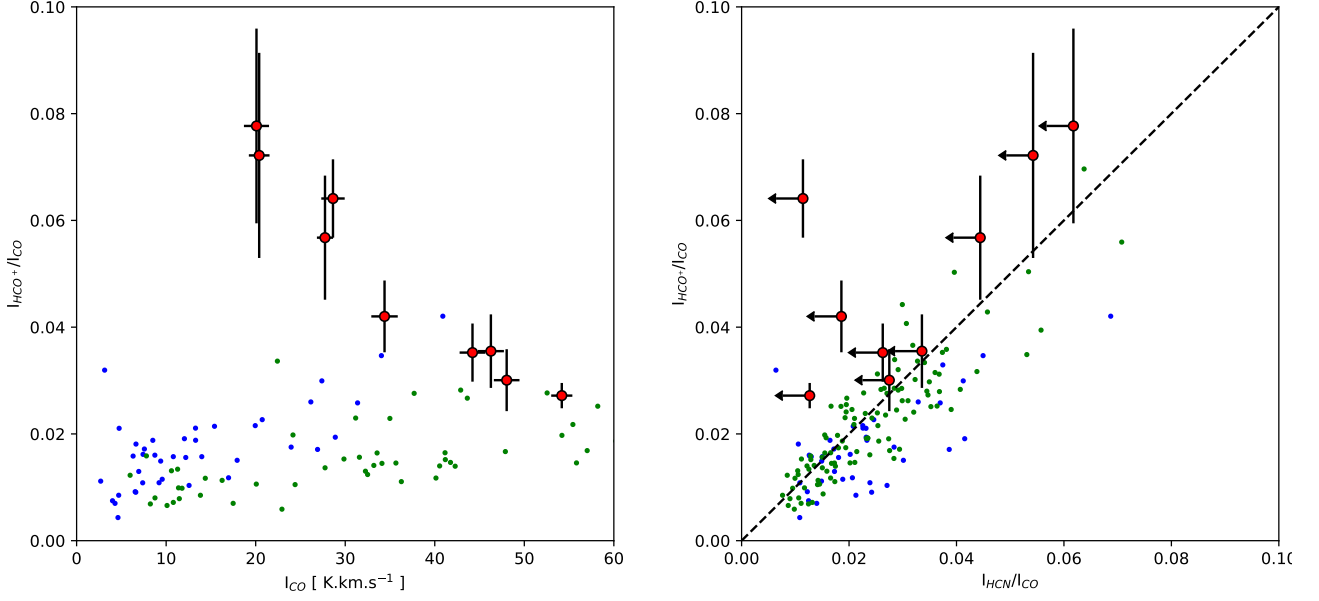


Fig. 2:  $I_{\text{HCO}^+}/I_{\text{CO}}$  as a function of  $I_{\text{CO}}$  (left) and  $I_{\text{HCN}}/I_{\text{CO}}$  (right). The red points are the clumps in Table 2, the blue and green points come from the EMPIRE (Jiménez-Donaire et al. 2019) and ALMOND surveys (Neumann et al. 2023). The dashed line in the right panel show the unity relation.

limit is not compatible with the predictions for the "dense" gas, suggesting that the detected HCO<sup>+</sup> emission is tracing diffuse molecular gas.

**Molecular gas mass** - 8/9 HCO<sup>+</sup> clumps seem to be unresolved with the present ALMA observations, for which the synthesised beam has a characteristic radius of 20 pc. The triplets  $\{N_{\text{X}}, n_{\text{H}}, T_{\text{kin}}\}$  from RADEX are average value for the total emission. Assuming spherical clouds, the average molecular gas mass of the clumps predicted by the models is  $M_{\text{pred}} = 8.3 \times 10^5 M_{\odot}$  for the "diffuse" gas abundances and  $M_{\text{pred}} = 8.3 \times 10^6 M_{\odot}$  for the "dense" gas abundances. Those estimates are larger than the average molecular gas mass derived from the CO emission with a standard CO-to-H<sub>2</sub> conversion factor:  $M_{\text{obs}} = 2.5 \times 10^5 M_{\odot}$ . This suggests that these 8 HCO<sup>+</sup> clumps are smaller than the beam of ALMA, and likely associated with diffuse gas.

**Total H<sub>2</sub> luminosity** - Cooling of the gas commonly occurs via H<sub>2</sub> emission. It is possible to estimate the total H<sub>2</sub> luminosity that a molecular cloud of radius  $R = 20$  pc would produce, assuming local thermal equilibrium (LTE):

$$L_{\text{H}_2} = 4\pi D_L^2 \Omega \left( \sum \frac{1}{4\pi} h\nu_{ij} A_{ij} N_i \right) \quad (3)$$

where  $\nu_{ij}$ ,  $A_{ij}$  are the frequency and the Einstein A coefficient of the H<sub>2</sub> transition  $i \rightarrow j$ ,  $D_L$  is the luminosity distance,  $\Omega$  is the solid angle of a clump of radius 20 pc, and  $N_i$  is the column density of H<sub>2</sub> molecules in the excitation level  $i$  given by:

$$N_i = N_{\text{tot}} \times \left( g_i \exp\left(\frac{-E_i}{kT_{\text{ex}}}\right) \right) / \left( \sum g_i \exp\left(\frac{-E_i}{kT_{\text{ex}}}\right) \right) \quad (4)$$

with  $g_i$ ,  $E_i$  the weight and energy of level  $i$ , and  $T_{\text{ex}}$  the excitation temperature. The total column density is estimated assuming a spherical cloud:

$$N_{\text{tot}} = \frac{(4/3)\pi n R^3}{4\pi R^2} \quad (5)$$

**Cooling by H<sub>2</sub>** - We predict that the total H<sub>2</sub> luminosity produced by a molecular cloud of radius 20 pc would be  $L_{\text{H}_2} = 2 \times 10^{28} -$

$3.7 \times 10^{37}$  erg.s<sup>-1</sup> if the gas is diffuse ( $n_{\text{H}} = 10^3$  cm<sup>-3</sup> and  $T_{\text{kin}} = T_{\text{ex}} = 20 - 125$  K), and  $L_{\text{H}_2} = 9.7 \times 10^{37} - 4.1 \times 10^{39}$  erg.s<sup>-1</sup> if the gas is dense ( $n_{\text{H}} = 10^4$  cm<sup>-3</sup> and  $T_{\text{kin}} = T_{\text{ex}} = 100 - 200$  K). We note that the H<sub>2</sub> luminosity is highly dependent on the gas temperature. Better constraints on the gas temperature are thus important, in particular for the diffuse gas solution. KMOS observation of ro-vibrational lines of H<sub>2</sub> will allow to measure the cooling energy radiated by H<sub>2</sub> (Salomé et al., in prep.). If the observed H<sub>2</sub> luminosity is smaller than  $10^{38}$  erg.s<sup>-1</sup>, we would be able to eliminate the dense gas solutions, and constrain the gas temperature, i.e.  $L_{\text{H}_2} = 3.4 \times 10^{30}$  erg.s<sup>-1</sup> at 25 K,  $7.1 \times 10^{34}$  erg.s<sup>-1</sup> at 50 K,  $1.6 \times 10^{36}$  erg.s<sup>-1</sup> at 75 K, and  $9.7 \times 10^{36}$  erg.s<sup>-1</sup> at 100 K.

**Heating by the radio jet** - The northern radio emission of Centaurus is complex with several structures extended to different scale. Neff et al. (2015) estimated the total power within the different structures and reported a power  $P_{\text{NML}} \sim 10^{44}$  erg.s<sup>-1</sup> for the Northern Middle Lobe over an area of 425 kpc<sup>2</sup>. If we consider an homogeneously distributed power within the Northern Middle Lobe, the H<sub>2</sub> emission produced by the "dense" gas would be at least 30% of the power of the radio plasma available locally at the scale of the clumps. In particular, this fraction is higher than unity for a gas temperature higher than 120 K. This suggests that the energy of the Northern Inner Lobe is not enough to heat dense gas at  $n_{\text{H}} = 10^4$  cm<sup>-3</sup>. Conversely, this fraction would be only 3% for "diffuse" gas at 100 K. The energy injected by the radio-jet is thus quantitatively a possible source of excitation of the H<sub>2</sub>.

**Cosmic ray heating** - In the case of heating by cosmic rays (Yusef-Zadeh et al. 2007; Ferland et al. 2008), we can estimate the cosmic-ray ionisation rate  $\zeta$  needed to balance the cooling by the H<sub>2</sub> line emission. We consider two cases representative of the "diffuse" and "dense" gas conditions predicted by RADEX: (i)  $n_{\text{H}} = 10^3$  cm<sup>-3</sup> and  $T_{\text{kin}} = T_{\text{ex}} = 75$  K, (ii)  $n_{\text{H}} = 10^4$  cm<sup>-3</sup> and  $T_{\text{kin}} = T_{\text{ex}} = 150$  K. Using the molecular gas mass and the total H<sub>2</sub> luminosity predicted by RADEX, the average total line emission per H<sub>2</sub> molecule would be  $\mathcal{L}_{\text{H}_2} = 3.2 \times 10^{-34}$  W.H<sub>2</sub><sup>-1</sup> for the "diffuse" gas and  $\mathcal{L}_{\text{H}_2} = 2.0 \times 10^{-32}$  W.H<sub>2</sub><sup>-1</sup> for the "dense" gas.

Following the discussion of [Ogle et al. \(2010\)](#), we estimated the cosmic ray ionisation rate using the following equation:

$$\zeta = 1.2 \times 10^{-13} \times \left( \frac{\mathcal{L}_{H_2}}{1.3 \times 10^{-31} \text{ W}} \right) s^{-1} . H^{-1} \quad (6)$$

To balance the  $H_2$  cooling with cosmic ray heating, a ionisation rate  $\zeta = 3.0 \times 10^{-16} s^{-1} . H^{-1}$  and  $1.9 \times 10^{-14} s^{-1} . H^{-1}$  is required for the "diffuse" and "dense" gas, respectively. This is at least a factor of 0.4 and 24 times, respectively, the cosmic ray ionisation rate derived in the centre of Centaurus A by [Van der Tak et al. \(2016\)](#). This suggests that heating of the molecular gas within the filaments is unlikely dominated by the cosmic rays.

Table 4: Cosmic ray heating predicted by RADEX, assuming LTE. We considered two set of parameters characteristics of the diffuse and dense gas.

$n_H$ ( $\text{cm}^{-3}$ )	$T_{\text{ex}}$ (K)	$L_{H_2}$ ( $\text{erg} . s^{-1}$ )	$\mathcal{L}_{H_2}$ ( $\text{W} . H_2^{-1}$ )	$\zeta$ ( $s^{-1} . H^{-1}$ )
$10^3$	75	$1.6 \times 10^{36}$	$3.2 \times 10^{-34}$	$3.0 \times 10^{-16}$
$10^4$	150	$1.0 \times 10^{39}$	$2.3 \times 10^{-32}$	$1.9 \times 10^{-14}$

*Possible origin of the  $HCO^+$  emission* - At densities  $n \leq 10^4 \text{ cm}^{-3}$ , high  $I_{HCO^+}/I_{HCN}$  line ratios can be explained by photo-dissociated regions (PDRs) or X-ray dominated regions (XDRs; [Meijerink et al. 2007](#)). In particular, the line ratios between dense gas tracers found in the nuclear region of NGC 5128 by [McCoy et al. \(2017\)](#) indicate that the  $HCO^+$  might comes from XDR.  $HCO^+$  emission can also be enhanced by shocks in the diffuse gas ([Godard et al. 2019](#)) and there is several evidence of shocks in the filaments of Centaurus A ([Oosterloo & Morganti 2005](#); [Salomé et al. 2016a, 2019](#)). Studying the presence of PDR, XDR or shocks in the northern filaments of Centaurus A is out of the scope of the present paper and would need additional observational constraints. In particular,  $H_2$  ro-vibrational lines can identify the relative contribution of shocks and PDR to the energy injection within the molecular gas ([Villa-Vélez et al. 2024](#)).

## 6. Conclusion and discussion

We have presented the first observations of the  $HCN(1-0)$ ,  $HCO^+(1-0)$  and  $SiO(2-1)$  emission in the northern filaments of Centaurus A conducted with ALMA.  $HCO^+(1-0)$  is detected in 9 clumps distributed along the Horseshoe complex but no  $HCN$ ,  $SiO$  is detected. We extracted the spectra of the clumps for the  $HCO^+(1-0)$  and  $CO(1-0)$  emission, and computed upper limits of the  $HCN(1-0)$ ,  $SiO(2-1)$  fluxes within the  $2\sigma$  contours of the  $HCO^+$  moment 0 map. We derived high  $I_{HCO^+}/I_{CO}$ ,  $I_{HCO^+}/I_{HCN}$  line ratios and a low  $I_{HCN}/I_{CO}$  ratio, compared to that typically observed in nearby star-forming galaxies. Moreover, we found that the  $I_{HCO^+}/I_{CO}$  ratio decreases with increasing  $I_{CO}$ . This indicates an enhanced  $HCO^+$  emission that is likely not associated with a high dense gas fraction.

We used the average  $CO(1-0)$  and  $HCO^+(1-0)$  integrated intensity, as well as the upper limit on  $I_{HCN}$  to constrain grid of large velocity gradient models from RADEX. The observations can be explained either by "diffuse" molecular gas at  $n_H = 10^3 \text{ cm}^{-3}$  or by "dense" molecular gas at  $n_H = 10^4 \text{ cm}^{-3}$ . However, we note that "dense" molecular gas is not compatible with the upper limit on  $I_{SiO}$ . Moreover, an analysis of the predicted molecular gas mass and  $H_2$  luminosity suggests that the  $HCO^+(1-0)$  likely arise from "diffuse" gas at  $n \leq 10^3 \text{ cm}^{-3}$ .

*Acknowledgements.* We thank the referee for his/her comments. ALMA is a partnership of ESO (representing its member states), NSF (USA)

and NINS (Japan), together with NRC (Canada), NSC and ASIAA (Taiwan), and KASI (Republic of Korea), in cooperation with the Republic of Chile. The Joint ALMA Observatory is operated by ESO, AUI/NRAO and NAOJ. QS thanks the Observatoire de Paris for the access to the computational facilities. Q.S. acknowledges the financial support from the visitor and mobility program of the Finnish Centre for Astronomy with ESO (FINCA), funded by the Academy of Finland grant nr 306531.

## References

- Alatalo, K. 2015, *ApJ*, 801, L17  
Auld, R., Smith, M. W. L., Bendo, G., et al. 2012, *MNRAS*, 420, 1882  
Barcos-Muñoz, L., Aalto, S., Thompson, T. A., et al. 2018, *ApJL*, 853, L28  
Blanco, V. M., Graham, J. A., Lasker, B. M., & Osmer, P. S. 1975, *ApJ*, 198, L63  
Bower, R. G., Benson, A. J., Malbon, R., et al. 2006, *MNRAS*, 370, 645  
Brouillet, N., Muller, S., Herpin, F., Braine, J., & Jacq, T. 2005, *A&A*, 429, 153  
Capetti, A., Balmaverde, B., Tadhunter, C., et al. 2022, *A&A*, 657, A114  
Cicone, C., Maiolino, R., Aalto, S., Muller, S., & Feruglio, C. 2020, *A&A*, 633, A163  
Croft, S., van Breugel, W., de Vries, W., et al. 2006, *ApJ*, 647, 1040  
Croton, D. J., Springel, V., White, S. D. M., et al. 2006, *MNRAS*, 365, 11  
Duncan, K. J., Windhorst, R. A., Koekemoer, A. M., et al. 2023, *MNRAS*, 522, 4548  
Ferland, G. J., Fabian, A. C., Hatch, N. A., et al. 2008, *MNRAS*, 386, L72  
Flower, D. R. & Pineau des Forêts, G. 2015, *A&A*, 578, A63  
Forbrich, J., Lada, C. J., Pety, J., & Petitpas, G. 2023, *MNRAS*, 525, 5565  
Galamez, M., Schrubba, A., De Breuck, C., et al. 2020, *A&A*, 643, A63  
García-Rodríguez, A., Usero, A., Leroy, A. K., et al. 2023, *A&A*, 672, A96  
Godard, B., Falgarone, E., Gerin, M., Hily-Blant, P., & De Luca, M. 2010, *A&A*, 520, A20  
Godard, B., Pineau Des Forêts, G., Lesaffre, P., et al. 2019, *A&A*, 622, A100  
Harris, G. L. H., Rejkuba, M., & Harris, W. E. 2010, *PASA*, 27, 457  
Imanishi, M., Nakanishi, K., Tamura, Y., Oi, N., & Kohno, K. 2007, *AJ*, 134, 2366  
Jiménez-Donaire, M. J., Bigiel, F., Leroy, A. K., et al. 2019, *ApJ*, 880, 127  
Joseph, P., Sreekumar, P., Stalin, C. S., et al. 2022, *MNRAS*, 516, 2300  
Kohno, K. 2003, in *ASP Conference Proceedings*, Vol. 289 (ASP), 349  
Kohno, K. 2005, in *AIP Conference Proceedings*, Vol. 783 (AIP), 203–208  
Krips, M., Neri, R., García-Burillo, S., et al. 2008, *ApJ*, 677, 262  
Liszt, H. S., Pety, J., & Lucas, R. 2010, *A&A*, 518, A45  
Liu, X., Wang, J., & Xu, J. 2013, *MNRAS*, 431, 27  
McCoy, M., Ott, J., Meier, D. S., et al. 2017, *ApJ*, 851, 76  
Meijerink, R., Spaans, M., & Israel, F. P. 2007, *A&A*, 461, 793  
Morganti, R. 2010, *PASA*, 27, 463  
Morganti, R., Robinson, A., Fosbury, R. A. E., et al. 1991, *MNRAS*, 249, 91  
Neff, S. G., Eilek, J. A., & Owen, F. N. 2015, *ApJ*, 802, 87  
Nesvadba, N. P. H., Bicknell, G. V., Mukherjee, D., & Wagner, A. Y. 2020, *A&A*, 639, L13  
Neumann, L., Gallagher, M. J., Bigiel, F., et al. 2023, *MNRAS*, 521, 3348  
Ogle, P., Boulanger, F., Guillard, P., et al. 2010, *ApJ*, 724, 1193  
Oosterloo, T. A. & Morganti, R. 2005, *A&A*, 429, 469  
Pety, J., Guzmán, V. V., Orkisz, J. H., et al. 2017, *A&A*, 599, A98  
Privon, G. C., Herrero-Illana, R., Evans, A. S., et al. 2015, *ApJ*, 814, 39  
Rejkuba, M., Minniti, D., Silva, D. R., & Bedding, T. R. 2001, *A&A*, 379, 781  
Salas, P., Galaz, G., Salter, D., et al. 2014, *ApJ*, 797, 134  
Salomé, Q., Salomé, P., & Combes, F. 2015, *A&A*, 574, A34  
Salomé, Q., Salomé, P., Combes, F., & Hamer, S. 2016a, *A&A*, 595, A65  
Salomé, Q., Salomé, P., Combes, F., Hamer, S., & Heywood, I. 2016b, *A&A*, 586, A45  
Salomé, Q., Salomé, P., Gusdorf, A., & Combes, F. 2019, *A&A*, 627, A6  
Salomé, Q., Salomé, P., Miville-Deschênes, M., Combes, F., & Hamer, S. 2017, *A&A*, 608, A98  
Schiminovich, D., van Gorkom, J. H., van der Hulst, J. M., & Kasow, S. 1994, *ApJ*, 423, L101  
Schirm, M. R. P., Wilson, C. D., Madden, S. C., & Clements, D. L. 2016, *ApJ*, 823, 87  
Snow, T. P. & McCall, B. J. 2006, *ARA&A*, 44, 367  
Towner, A. P. M., Ginsburg, A., Dell’Ova, P., et al. 2024, *ApJ*, 960, 48  
van der Tak, F. F. S., Black, J. H., Schöier, F. L., Jansen, D. J., & van Dishoeck, E. F. 2007, *A&A*, 468, 627  
Van der Tak, F. F. S., Weiß, A., Liu, L., & Güsten, R. 2016, *A&A*, 593, A43  
Villa-Vélez, J. A., Godard, B., Guillard, P., & Pineau des Forêts, G. 2024, *arXiv:2405.02058 [arXiv:2405.02058]*  
Walter, F., Bolatto, A. D., Leroy, A. K., et al. 2017, *ApJ*, 835, 265  
Yusef-Zadeh, F., Wardle, M., & Roy, S. 2007, *ApJ*, 665, L123  
Zovaro, H. R. M., Sharp, R., Nesvadba, N. P. H., et al. 2020, *MNRAS*, 499, 4940

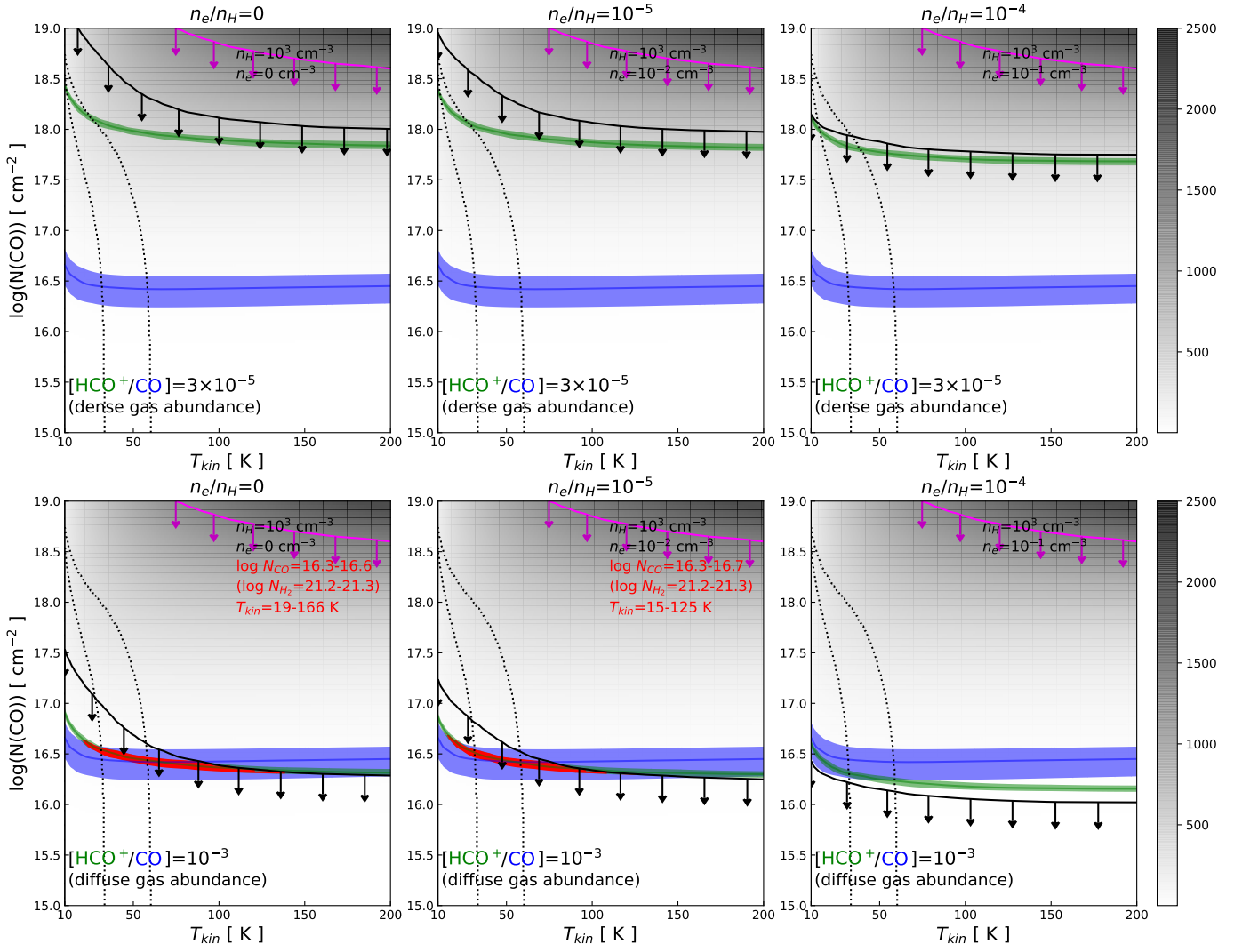


**Fig. 3: Radiative transfer predictions from RADEX** for an HCO<sup>+</sup>/CO abundance ratio typical of the dense (*top*) and diffuse gas (*bottom*). The blue and green areas show the range of observed CO(1–0) and HCO<sup>+</sup>(1–0) integrated intensities, while the black and magenta line indicate the upper limits of HCN(1–0) and SiO(2–1). The columns correspond to predictions for a relative electron abundance  $n_e/n_H = 0$  (left),  $n_e/n_H = 10^{-5}$  (middle),  $n_e/n_H = 10^{-4}$  (right). The red area correspond to the models that reproduce the CO and HCO<sup>+</sup> intensities and the HCN upper limit. The dot lines indicate the models that reproduce the mid-J CO lines emission from [Salomé et al. \(2019\)](#).

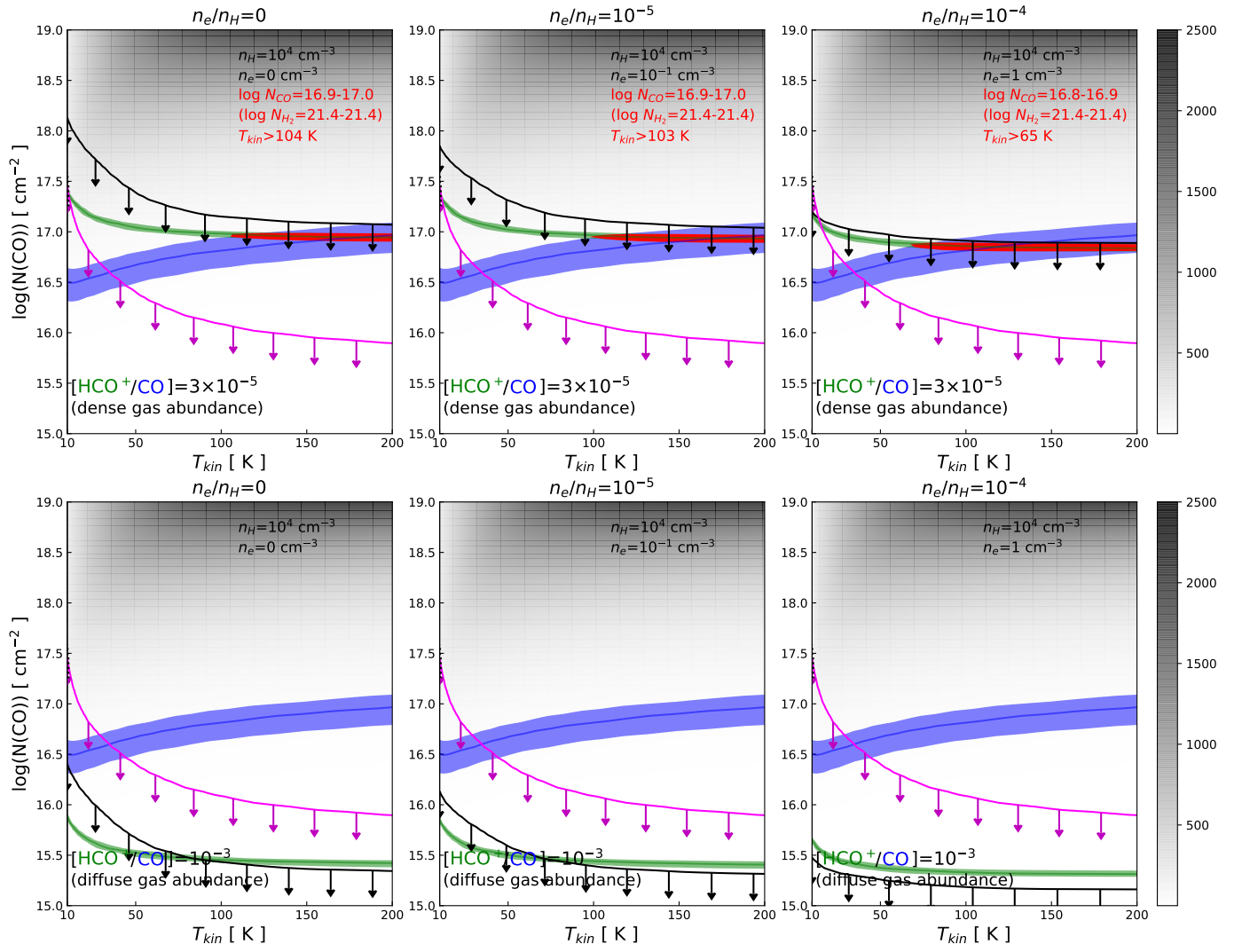


Fig. 3 (continued)

**Appendix A:  $\text{HCO}^+$  clumps - spectra**

**Appendix B: Variation of the relative abundances**

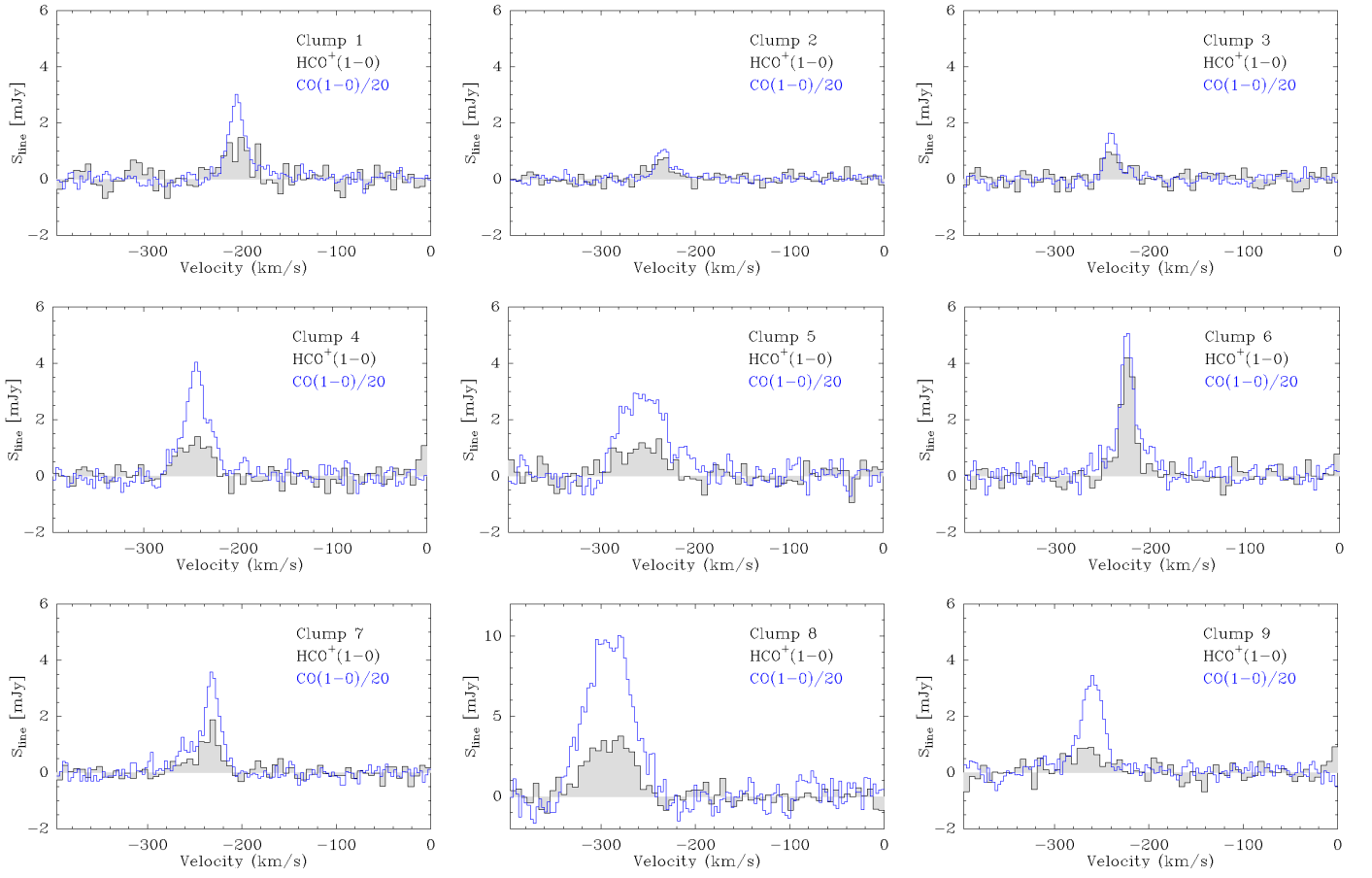


Fig. A.1: **Individual clumps.** Integrated spectra of the  $\text{HCO}^+(1-0)$  (black) and  $\text{CO}(1-0)$  emission (blue). The  $\text{CO}(1-0)$  is scaled by a factor of 20. The velocities are relative to the systemic velocity of Centaurus A.

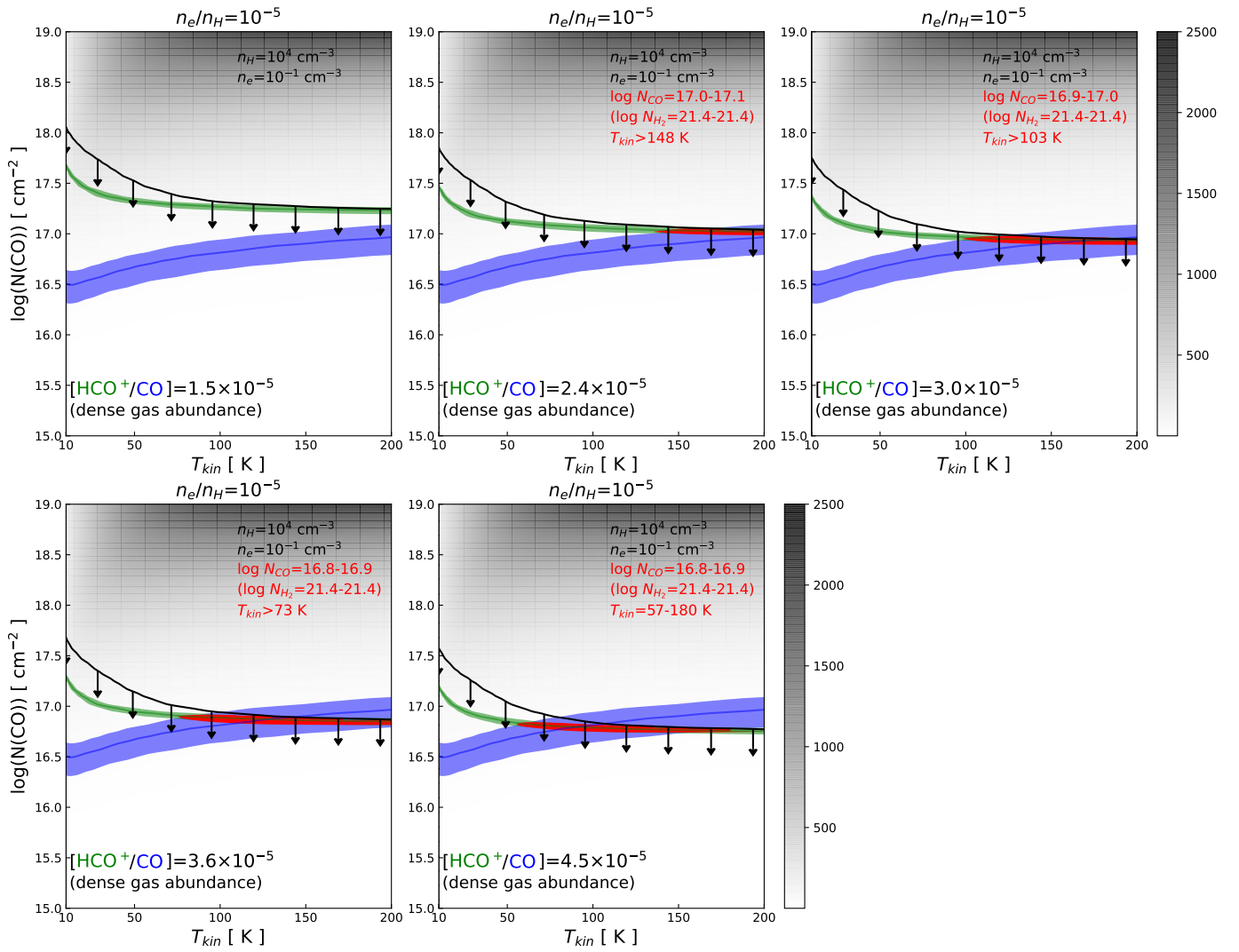


Fig. B.1: **Radiative transfer predictions from RADEX** for dense gas at  $n_{\text{H}} = 10^4$ , with a relative electron abundance  $n_{\text{e}}/n_{\text{H}} = 10^{-5}$ . The HCO<sup>+</sup>/CO abundance ratio is respectively 50, 80, 100, 120, 150% of the typical value for the dense gas. The blue, green and red areas, and the black line are the same as in Figure 3.

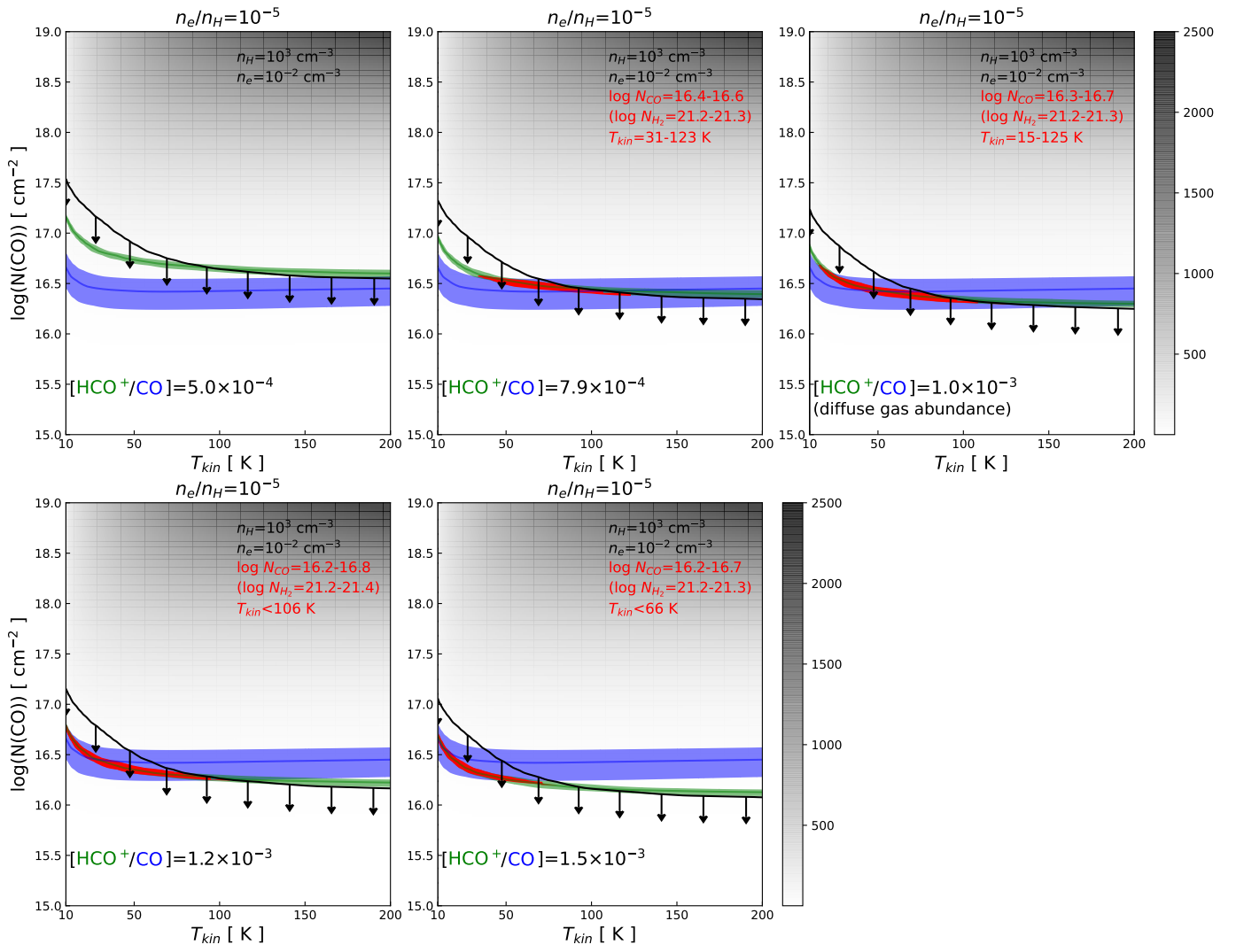


Fig. B.2: Same as Figure Fig. B.1 for diffuse gas at  $n_{\text{H}} = 10^3$ .